Earth's Future

Supporting Information for

Reduced rainfall in future heavy precipitation events related to contracted rainy area despite increased rain rate

Moshe Armon[1], Francesco Marra[2], Yehouda Enzel[1], Dorita Rostkier-Edelstein[1,3], Chaim I. Garfinkel[1], Ori Adam[1], Uri Dayan[4], Efrat Morin[1]

[1]Fredy and Nadine Herrmann Institute of Earth Sciences, the Hebrew University of Jerusalem, Jerusalem, 9190401, Israel

[2]National Research Council of Italy, Institute of Atmospheric Sciences and Climate, CNR-ISAC, Bologna 40129, Italy

[3]Department of Environmental Physics, Environmental Sciences Division, IIBR, Ness-Ziona 7410001, Israel

[4]Department of Geography, the Hebrew University of Jerusalem, Jerusalem, 9190401, Israel

Contents of this file

Additional Supporting Information (Files uploaded separately)

Text S1. Brief analysis of the climate change applied for PGW simulations

The changes applied, under the RCP 8.5 scenario, represent a major warming of the region. At the ground level a larger temperature increase is seen over land than over the sea with local maxima over the Arabian Peninsula and north-western Asia (Fig. S1a). The warming peaks at the upper troposphere (~300 hPa), where maximum values are near the equator, and is stronger in fall compared to spring (Fig. S1b-c). It is interesting to note that the warming in the upper troposphere is enhanced during fall, which may increase the static stability compared to winter and spring. The pattern of sea level pressure resembles the surface temperature change (with an opposite sign) and exhibits a maximum over the central Mediterranean, and a minimum at the Arabian Peninsula and north-western Asia, implying a decreased frequency of MCs, or a general decrease in sea-land pressure gradient. These changes are in concert with previous studies (e.g., Giorgi and Lionello, 2008; Seager et al., 2019; Tuel et al., 2021; Tuel and Eltahir, 2020). The moisture field is only slightly increased over the Mediterranean region, with larger increases in fall than in spring, and farther to the south in equatorial Africa (Fig. S1b,d). Combined with decreased zonal wind at both the lower and the upper tropopause, this suggests a decrease in moisture flux into the eastern Mediterranean.

Table S1: Heavy precipitation events (HPEs) analysed in this study. Further details on the identification of events are described in Armon et al. (2020). Durations for which each of the HPEs were identified are marked with and X.

HPE #	Start time*	End time*	Synoptic classification[#]	HPE duration [h]						
				1	3	6	12	24	48	72
1	2-11-1991 9:00	5-11-1991 9:00	MC	X	X	X	X	X	X	X
2	22-2-1992 8:00	27-2-1992 21:00	MC						X	X
3	23-11-1992 9:00	26-11-1992 7:00	MC	X	X	X	X			
4	12-12-1992 14:00	18-12-1992 13:00	MC	X	X	X	X	X	X	X
5	31-3-1993 9:00	2-4-1993 2:00	ARST			X				
6	21-12-1993 12:00	23-12-1993 15:00	ARST						X	
7	21-2-1994 19:00	25-2-1994 0:00	MC		X	X	X			
8	1-11-1994 15:00	7-11-1994 13:00	ARST	X	X	X	X	X	X	X
9	14-11-1994 1:00	18-11-1994 5:00	MC	X	X	X	X	X	X	X
10	15-12-1994 12:00	20-12-1994 21:00	MC	X	X			X	X	X
11	28-12-1994 10:00	31-12-1994 23:00	MC			X				
12	4-2-1995 8:00	9-2-1995 10:00	MC					X	X	X
13	1-11-1995 11:00	3-11-1995 14:00	MC	X	X					
14	7-11-1995 10:00	10-11-1995 17:00	MC							X
15	6-3-1996 13:00	8-3-1996 4:00	MC		X	X	X	X	X	
16	11-12-1996 14:00	14-12-1996 15:00	ARST	X	X	X	X	X	X	X
17	13-1-1997 11:00	17-1-1997 7:00	MC	X	X	X	X	X	X	X
18	3-3-1997 6:00	4-3-1997 16:00	MC	X	X	X	X			
19	19-10-1997 11:00	20-10-1997 10:00	MC		X	X	X			
20	25-11-1997 10:00	27-11-1997 9:00	ARST		X	X	X	X		
21	4-4-1998 4:00	4-4-1998 17:00	MC			X	X			
22	28-12-1998 6:00	31-12-1998 21:00	MC	X	X	X	X	X		
23	13-12-1999 6:00	15-12-1999 8:00	MC	X	X	X	X			
24	18-1-2000 6:00	24-1-2000 2:00	MC		X	X	X	X	X	X
25	25-1-2000 15:00	28-1-2000 20:00	MC	X	X	X	X	X	X	X
26	12-2-2000 22:00	16-2-2000 16:00	MC	X	X	X	X	X	X	X
27	29-11-2000 0:00	1-12-2000 10:00	MC				X	X	X	X
28	19-12-2000 6:00	21-12-2000 17:00	MC	X	X					
29	30-4-2001 9:00	2-5-2001 17:00	MC	X	X	X	X	X	X	X
30	9-12-2002 6:00	12-12-2002 6:00	MC		X	X	X	X	X	X
31	2-1-2003 16:00	4-1-2003 12:00	MC		X	X				
32	27-1-2003 10:00	30-1-2003 13:00	MC	X	X	X	X	X		X
33	3-2-2003 0:00	5-2-2003 16:00	MC				X	X	X	
34	17-2-2003 19:00	22-2-2003 23:00	MC						X	X
35	24-2-2003 1:00	28-2-2003 2:00	MC				X	X	X	X
36	1-12-2003 14:00	5-12-2003 20:00	ARST	X	X	X	X	X	X	X
37	14-12-2003 16:00	15-12-2003 10:00	MC	X	X	X	X	X		
38	15-12-2005 15:00	18-12-2005 9:00	MC		X	X	X			
39	18-12-2007 14:00	21-12-2007 8:00	MC			X	X	X	X	
40	2-1-2008 3:00	5-1-2008 19:00	MC		X	X	X	X	X	X
41	17-1-2010 16:00	22-1-2010 6:00	MC	X	X	X	X	X	X	X

*Local winter time (UTC+2), presented as day-month-year and hour.
[#]Simplified synoptic classification is based on Alpert et al. (2004) as described by Armon et al. (2020).

Table S2: WRF model settings and specifications.

	Outer nest	Middle nest	Inner nest
Domains			
Spatial resolution [km]	25 x 25	5 x 5	1 x 1
Temporal resolution [s]	~100	~20	4-8
Domain size [pixels]	100 x 100	221 x 221	551 x 551
Number of vertical layers	68	68	68
Model top [hPa]	25	25	25
Physics			
Cumulus scheme	Tiedtke (Tiedtke, 1989; Zhang et al., 2011)		-
Microphysical scheme	Thompson (Thompson et al., 2008)		
Radiative transfer scheme	RRTMG Shortwave and Longwave (Iacono et al., 2008)		
Planetary boundary layer scheme	Mellor–Yamada– Janjić (Janjić, 1994)		
Surface layer scheme	Eta Similarity Scheme (Janjić, 1994)		
Land surface model	Unified Noah Land Surface (Tewari et al., 2004)		
Input data			
Historic simulations	ERA-Interim reanalysis (Dee et al., 2011)		
"Future" (PGW) simulation	ERA-Interim + Δ climate from CMIP5 models		

Table S3: Coupled Model Intercomparison Project phase 5 (CMIP5) models used to compute the ensemble mean climate.

#	Model name	Latitude resolution [°]	Longitue resolution [°]	Number of vertical levels	Model top [hPa]
1	ACCESS1-0	1.25	1.88	17	10
2	ACCESS1-3	1.25	1.88	17	10
3	CCSM4	0.94	1.25	17	10
4	CESM1-BGC	0.94	1.25	17	10
5	CESM1-CAM5	0.94	1.25	17	10
6	CMCC-CESM	3.68	3.75	27	1
7	CNRM-CM5	1.39	1.41	17	10
8	CanESM2	2.77	2.81	22	1
9	GFDL-CM3	2.00	2.50	23	1
10	GFDL-ESM2G	1.52	2.50	17	10
11	GFDL-ESM2M	1.52	2.50	17	10
12	GISS-E2-H	2.00	2.50	17	10
13	GISS-E2-R	2.00	2.50	17	10
14	HadGEM2-AO	1.25	1.88	17	10
15	HadGEM2-ES	1.25	1.88	17	10
16	IPSL-CM5A-LR	1.89	3.75	17	10
17	IPSL-CM5A-MR	1.27	2.50	17	10
18	IPSL-CM5B-LR	1.89	3.75	17	10
19	MIROC-ESM	2.77	2.81	29	1
20	MIROC-ESM-CHEM	2.77	2.81	29	1
21	MIROC5	1.39	1.41	17	10
22	MPI-ESM-LR	1.85	1.88	22	1
23	MPI-ESM-MR	1.85	1.88	22	1
24	MRI-CGCM3	1.11	1.13	22	1
25	MRI-ESM1	1.11	1.13	22	1
26	NorESM1-M	1.89	2.50	17	10
27	NorESM1-ME	1.89	2.50	17	10
28	bcc-csm1-1	2.77	2.81	17	10
29	inmcm4	1.50	2.00	17	10

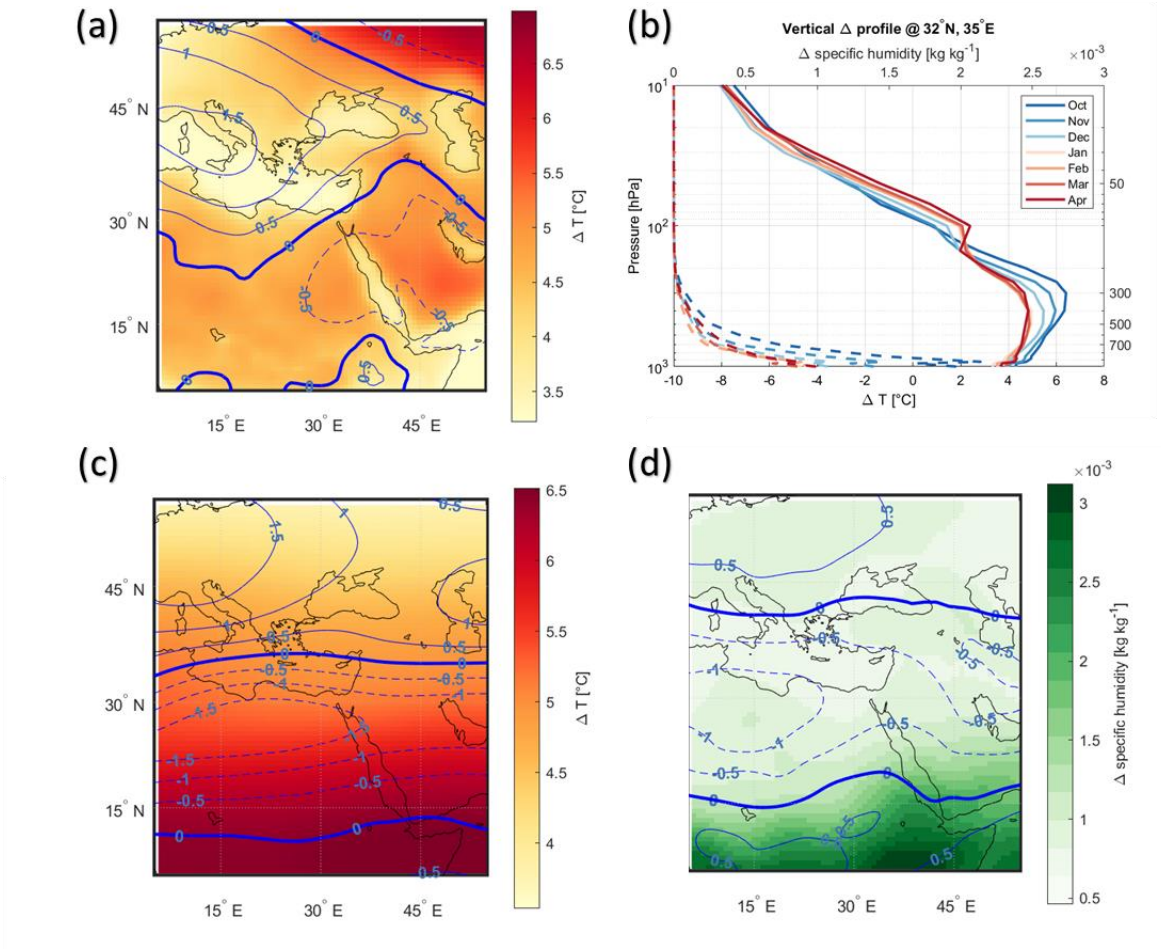

Figure S1. Examples of changes applied in "Future" (PGW) simulations based on ensemble mean of 29 CMIP5 models (Table S3). (a) Average change during the months with HPEs analyzed in this study (Oct through Apr; Table S1) in surface temperature (colors) and in sea-level pressure (contours). Dashed contours in panels a, c and d are negative signals. (b) Monthly vertical profiles of the change in temperature (solid lines, bottom horizontal axis) and in specific humidity (dashed lines, top horizontal axis) at the center of the study region (32°N, 35°E). Vertical changes were applied in each of the pixels along the study domain. (c) Average change (Oct through Apr) in upper-troposphere temperature (300 hPa; colors) and in the zonal (west-east) wind (contours). (d) Average change (Oct through Apr) in lower-troposphere specific humidity (850 hPa; colors) and in the zonal (west-east) wind (contours).

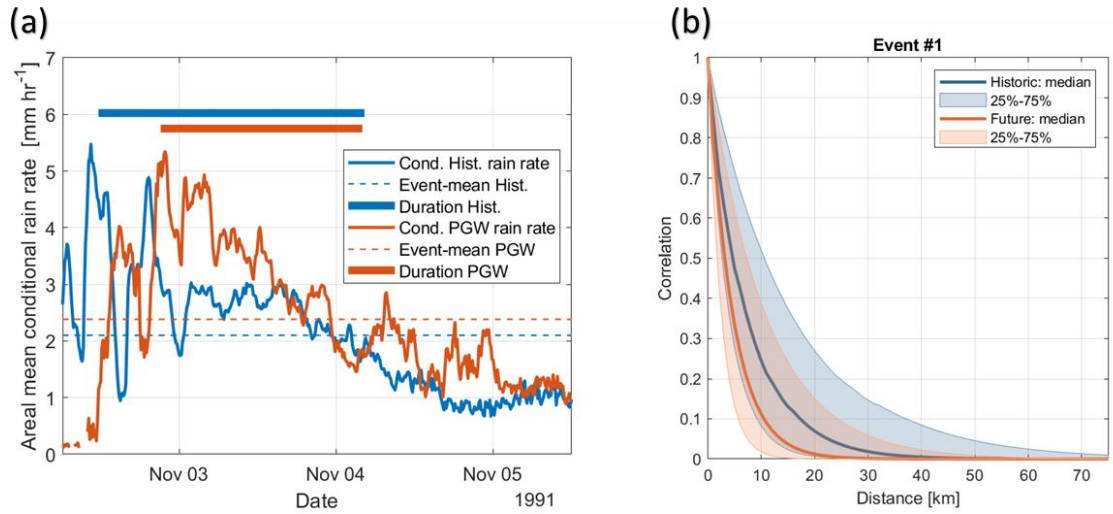

Figure S2. Additional rain properties of HPE #1. (a) Areal mean of 10-min conditional rain rates throughout the event. Dashed lines are the event-average values, and the bold, thick lines represent the duration of the event (the interval in which the central 90% of rainfall precipitated). (b) Autocorrelation structure of the 10-min convective rain fields for the first heavy precipitation event (HPE) in our collection, 2-5 Nov 1991. Curves are median values across 429 convective rain fields in the historic simulation (blue) and 407 in future simulation. Shaded areas represents the 25%-75% quantiles from each simulation.

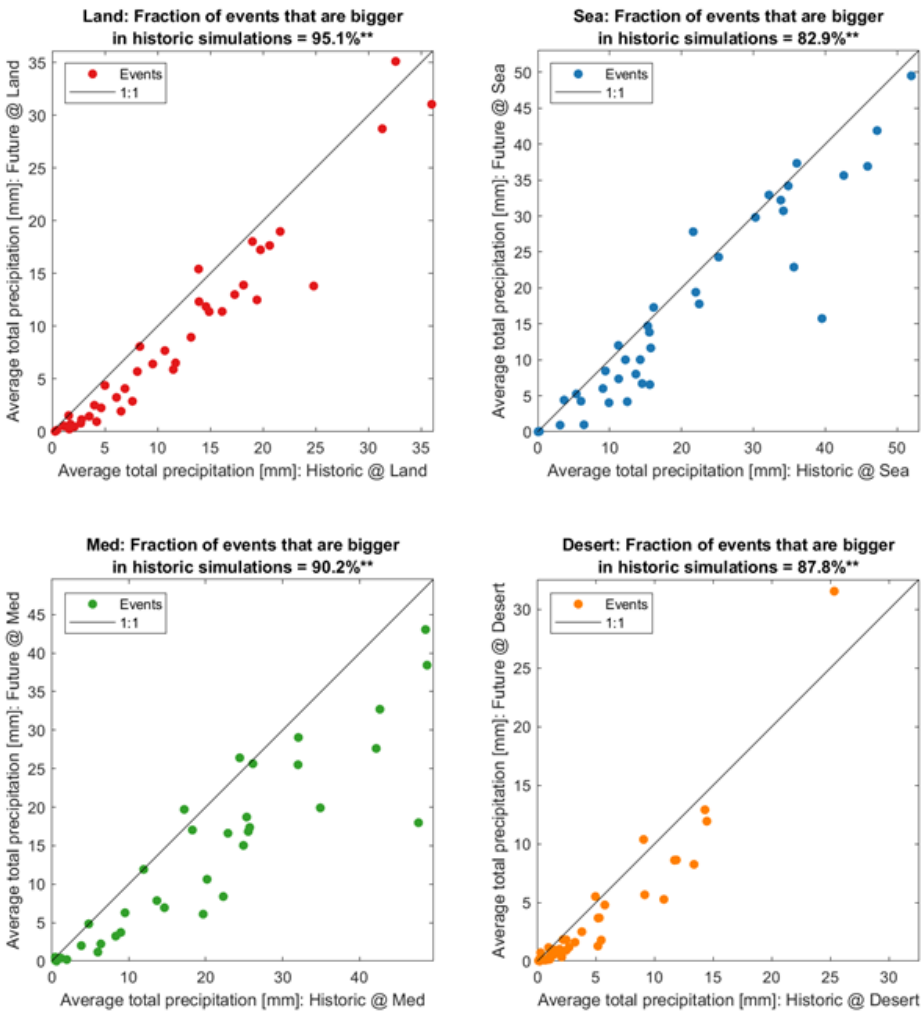

Figure S3. Comparison of future and historic rainfall accumulation of each of the 41 HPEs analyzed (as in Fig. 4a), computed separately for each of the sub-regions (Fig. 1b). Statistical significance, marked with ** in the panel titles, is based on paired (historic – future) tests (Sect. 2.4).

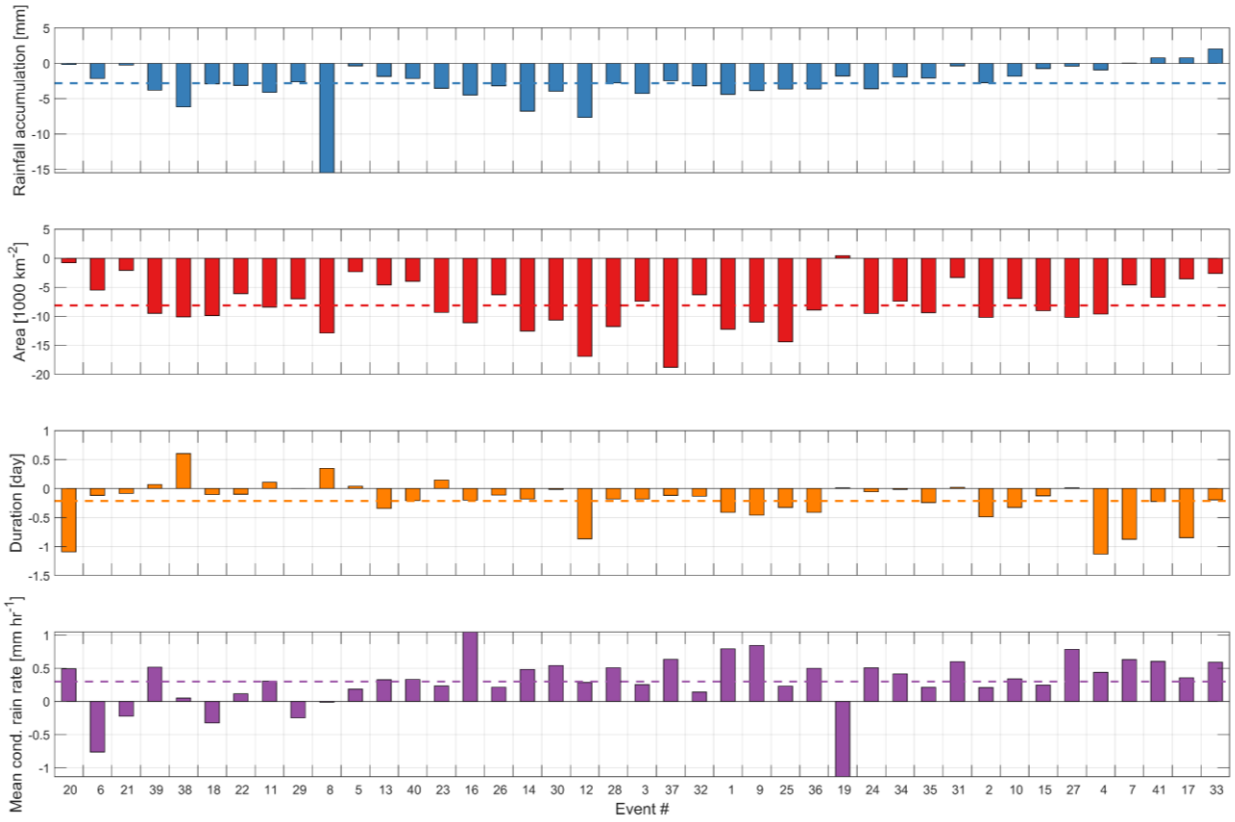

Figure S4. Change between future and historic simulations in event-average rainfall accumulation (blue), rainy area (red), event duration (orange), and mean conditional rain rate (purple), across the 41 HPEs analyzed. Events are ordered by their normalized changes in rainfall accumulation (see Fig. 5).

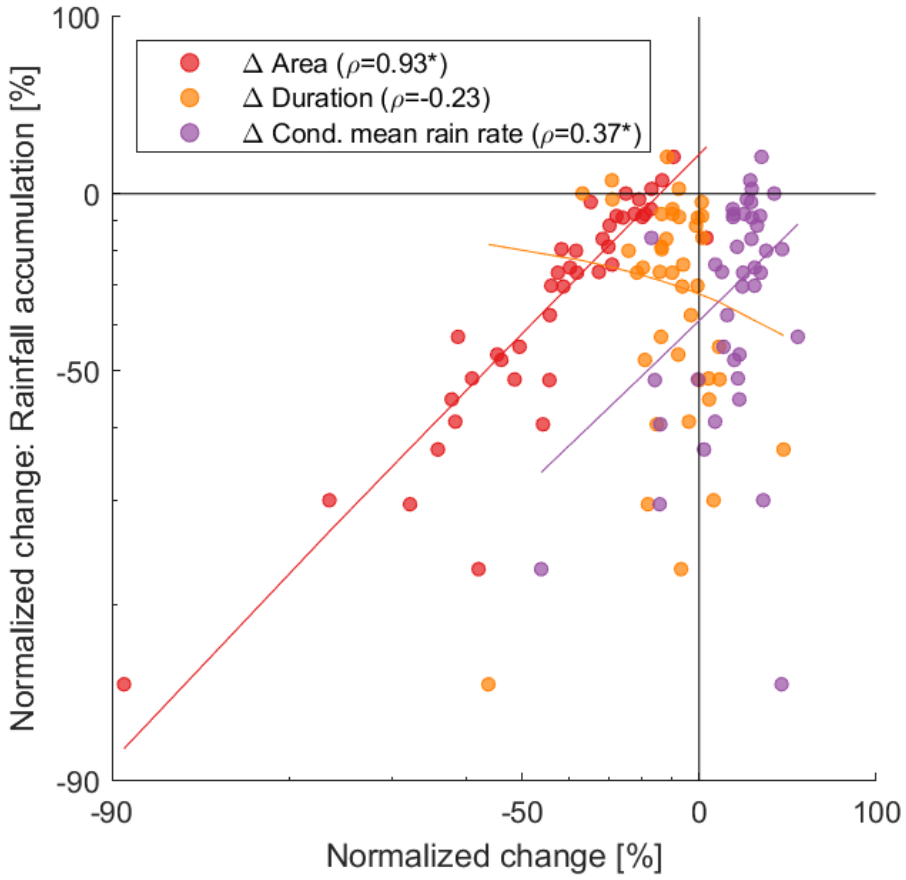

Figure S5. Association between the change in rainfall accumulation throughout the analyzed HPEs (vertical axis) and the different parameters shown in Fig. 5. Lines are the linear regressions between the parameters. Spearman's rank correlations are noted in the legend. Asterisks denote significant correlation.

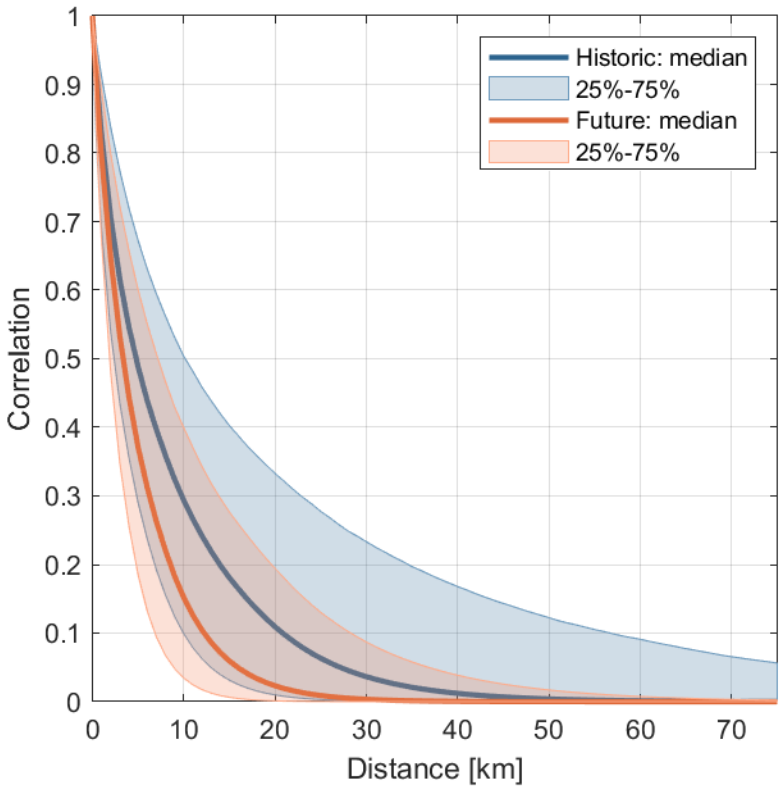

Figure S6. Spatial autocorrelation of the convective 10-min time steps for historic (blue) and future (orange) simulations. The number of convective time steps in historic and future simulations per event are 388±196 ($\mu \pm \sigma$) and 378±211, respectively. Calculations based on Marra and Morin (2018).

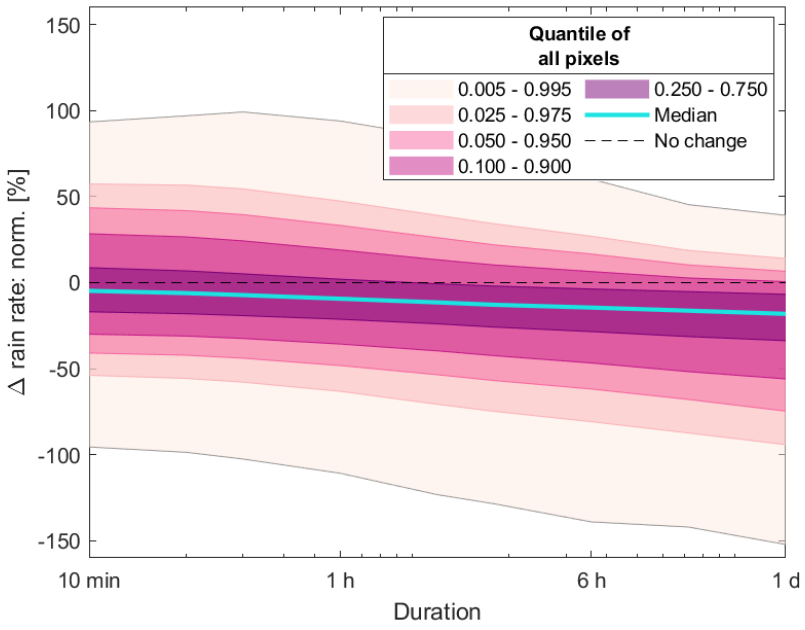

Figure S7. Quantiles among pixels (see Fig. 7) exhibiting different rain rate changes plotted versus the duration examined. Values are normalized to the areal mean value of each duration.

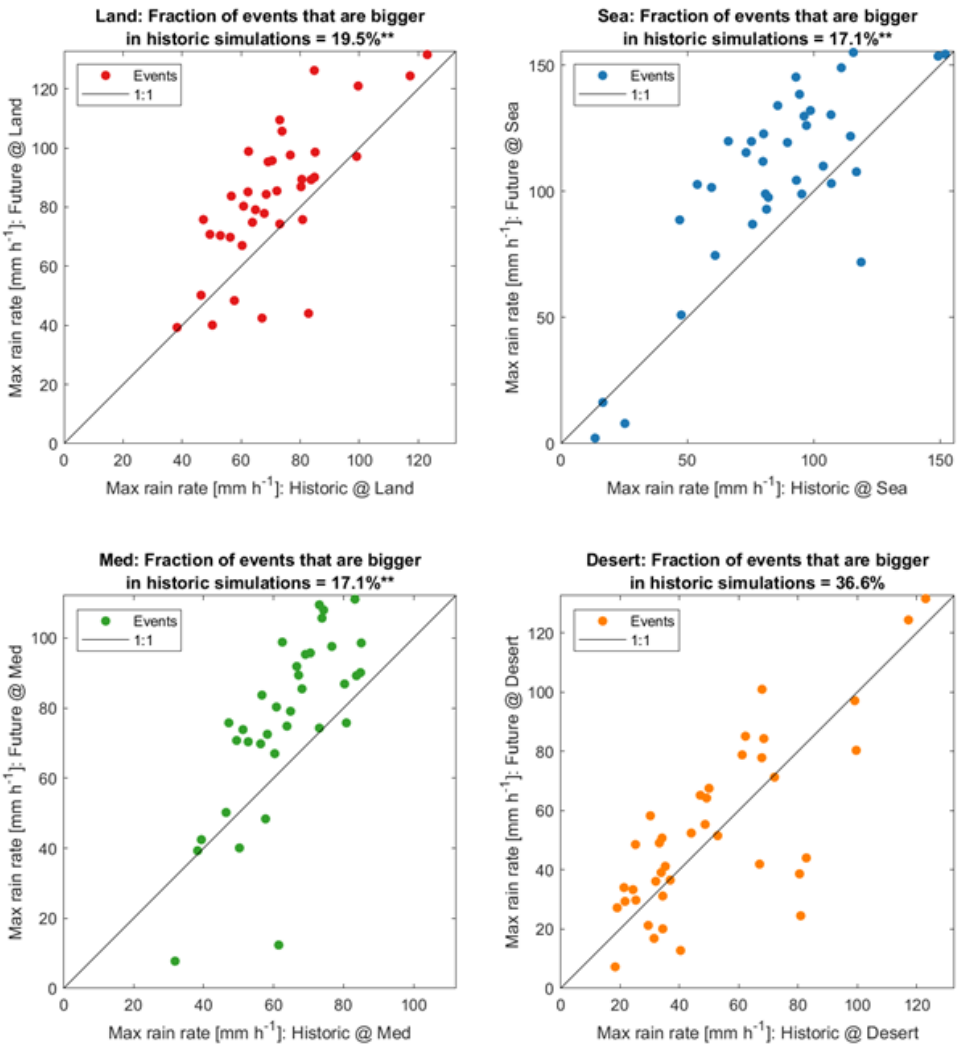

Figure S8. Same as in Fig. S3, but for maximal 10-min rain rate calculated throughout the pixels in each region and along all time steps. Maximum across all regions is in Fig. 4c.

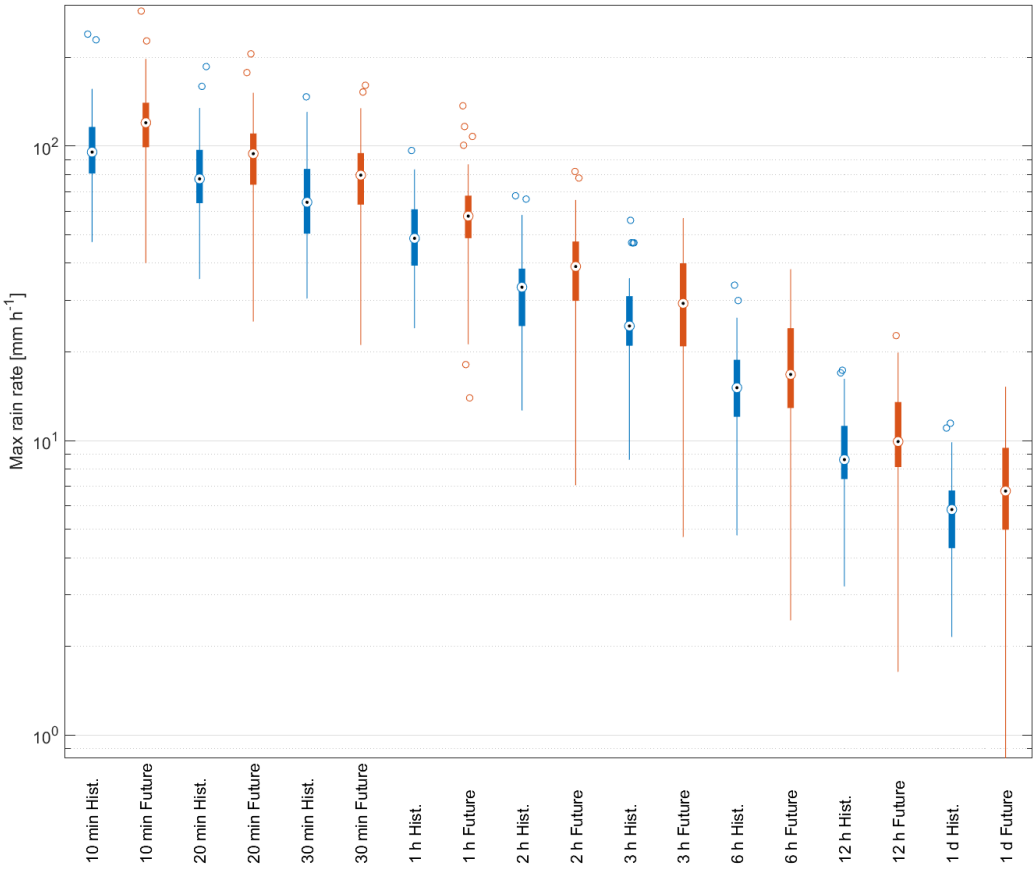

Figure S9. Boxplots of regionally maximal rain rates (across all pixels and time steps) for various durations. White circles with black dots are median values, boxes are the inter-quartile range (IQR), whiskers represents the full distribution except for cases where outliers (hollow circles) are found beyond the range of $\pm\, 1.5 \times IQR$ from the box.

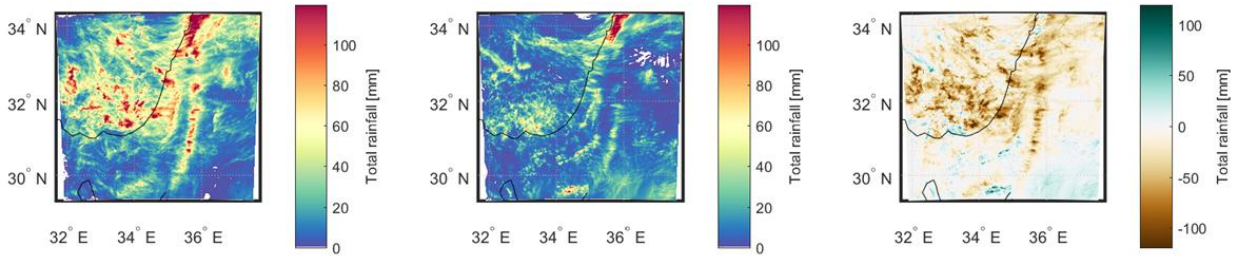

Figure S10. Rainfall in HPE#8 (1-7 Nov 1994). (a) Rainfall accumulation for the historic simulation (mean = 30.0 mm). (b) Total rainfall for the future (PGW) simulation (mean = 14.5 mm). (c) Difference between historic and future simulations (future – historic).

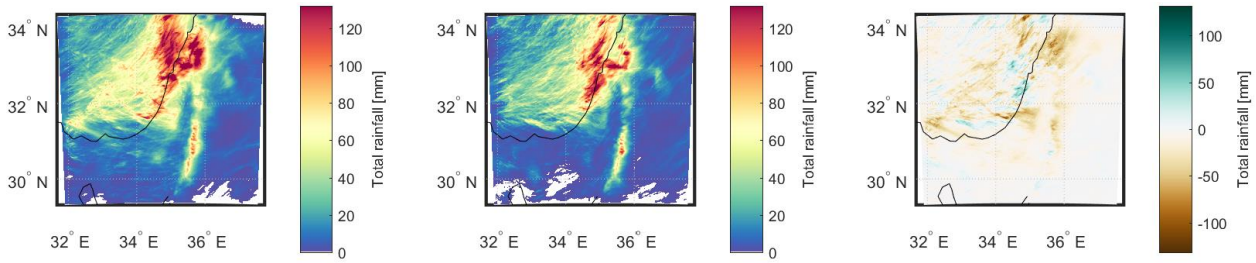

Figure S11. Same as figure S4, but for HPE#12 (4-9 Feb 1995). Historic simulation mean = 28.8 mm; future mean = 21.1 mm.

Movie S1. Animation of rain rate through time in historic (left) and future (right) simulations for HPE #1 (Table S1; Sect. 3.1).

Movie S2. Similar to Movie S1, but for HPE #8.

References from the Supporting Information

Alpert, P., Osetinsky, I., Ziv, B. and Shafir, H.: Semi-objective classification for daily synoptic systems: Application to the eastern Mediterranean climate change, Int. J. Climatol., 24(8), 1001–1011, doi:10.1002/joc.1036, 2004.

Armon, M., Marra, F., Enzel, Y., Rostkier-Edelstein, D. and Morin, E.: Radar-based characterisation of heavy precipitation in the eastern Mediterranean and its representation in a convection-permitting model, Hydrol. Earth Syst. Sci., 24(3), 1227–1249, doi:10.5194/hess-24-1227-2020, 2020.

Dee, D. P., Uppala, S. M., Simmons, A. J., Berrisford, P., Poli, P., Kobayashi, S., Andrae, U., Balmaseda, M. A., Balsamo, G., Bauer, P., Bechtold, P., Beljaars, A. C. M., van de Berg, L., Bidlot, J., Bormann, N., Delsol, C., Dragani, R., Fuentes, M., Geer, A. J., Haimberger, L., Healy, S. B., Hersbach, H., Hólm, E. V., Isaksen, L., Kållberg, P., Köhler, M., Matricardi, M., McNally, A. P., Monge-Sanz, B. M., Morcrette, J.-J., Park, B.-K., Peubey, C., de Rosnay, P., Tavolato, C., Thépaut, J.-N. and Vitart, F.: The ERA-Interim reanalysis: configuration and performance of the data assimilation system, Q. J. R. Meteorol. Soc., 137(656), 553–597, doi:10.1002/qj.828, 2011.

Giorgi, F. and Lionello, P.: Climate change projections for the Mediterranean region, Glob. Planet. Change, 63(2–3), 90–104, doi:10.1016/j.gloplacha.2007.09.005, 2008.

Iacono, M. J., Delamere, J. S., Mlawer, E. J., Shephard, M. W., Clough, S. A. and Collins, W. D.: Radiative forcing by long-lived greenhouse gases: Calculations with the AER radiative transfer models, J. Geophys. Res. Atmos., 113(D13), doi:10.1029/2008JD009944, 2008.

Janjić, Z. I.: The Step-Mountain Eta Coordinate Model: Further Developments of the Convection, Viscous Sublayer, and Turbulence Closure Schemes, Mon. Weather Rev., 122(5), 927–945, doi:10.1175/1520-0493(1994)122<0927:TSMECM>2.0.CO;2, 1994.

Marra, F. and Morin, E.: Autocorrelation structure of convective rainfall in semiarid-arid climate derived from high-resolution X-Band radar estimates, Atmos. Res., 200(September 2017), 126–138, doi:10.1016/j.atmosres.2017.09.020, 2018.

Nerini, D., Besic, N., Sideris, I., Germann, U. and Foresti, L.: A non-stationary stochastic ensemble generator for radar rainfall fields based on the short-space Fourier transform, Hydrol. Earth Syst. Sci., 21(6), 2777–2797, doi:10.5194/hess-21-2777-2017, 2017.

Seager, R., Osborn, T. J., Kushnir, Y., Simpson, I. R., Nakamura, J. and Liu, H.: Climate variability and change of mediterranean-type climates, J. Clim., 32(10), 2887–2915, doi:10.1175/JCLI-D-18-0472.1, 2019.

Tewari, M., Chen, F., Wang, W., Dudhia, J., LeMone, M. A., Mitchell, K., Ek, M., Gayno, G., Wegiel, J. and Cuenca, R. H.: Implementation and verification of the unified NOAH land surface model in the WRF model (Formerly Paper Number 17.5), in 20th Conference on Weather Analysis and Forecasting/16th Conference on Numerical Weather Prediction, pp. 11–15., 2004.

Thompson, G., Field, P. R., Rasmussen, R. M. and Hall, W. D.: Explicit Forecasts of Winter Precipitation Using an Improved Bulk Microphysics Scheme. Part II: Implementation of a New Snow Parameterization, Mon. Weather Rev., 136(12), 5095–5115, doi:10.1175/2008MWR2387.1, 2008.

Tiedtke, M.: A Comprehensive Mass Flux Scheme for Cumulus Parameterization in Large-Scale Models, Mon. Weather Rev., 117(8), 1779–1800, doi:10.1175/1520-0493(1989)117<1779:ACMFSF>2.0.CO;2, 1989.

Tuel, A. and Eltahir, E. A. B.: Why Is the Mediterranean a Climate Change Hot Spot?, J. Clim., 33(14), 5829–5843, doi:10.1175/JCLI-D-19-0910.1, 2020.

Tuel, A., O'Gorman, P. A. and Eltahir, E. A. B.: Elements of the Dynamical Response to Climate Change over the Mediterranean, J. Clim., 34(3), 1135–1146, doi:10.1175/JCLI-D-20-0429.1, 2021.

Zhang, C., Wang, Y. and Hamilton, K.: Improved Representation of Boundary Layer Clouds over the Southeast Pacific in ARW-WRF Using a Modified Tiedtke Cumulus Parameterization Scheme, Mon. Weather Rev., 139(11), 3489–3513, doi:10.1175/MWR-D-10-05091.1, 2011.